

High-field magnetic force microscopy as susceptibility imaging

Casey Israel, Weida Wu, and Alex de Lozanne^{a)}

Department of Physics, The University of Texas at Austin, 1 University Station C1600, Austin, Texas 78712

(Received 7 February 2006; accepted 25 May 2006; published online 17 July 2006)

We describe an extension of variable-temperature magnetic force microscopy (MFM) that allows spatial discrimination between the different states that exist in magnetically phase-separated materials. Some manganites exhibit a micrometer-scale separation of phases that are either ferromagnetic, paramagnetic, or antiferromagnetic. In an applied field large enough to saturate the ferromagnetic phase, any MFM contrast arising from the variation of the magnetization (domain walls, domains of differing orientation) is eliminated, while the nonferromagnetic phases are magnetized according to their susceptibilities. The different phases can then be discerned by their respective contrast levels in the MFM images. © 2006 American Institute of Physics.

[DOI: 10.1063/1.2221916]

Magnetic force microscopy (MFM) was developed as a scanning probe technique for mapping out magnetic field distributions on a microscopic scale.¹ Among other purposes, MFM has served as a valuable tool for the development of magnetic recording media,^{2,3} has been applied to patterned ferromagnetic materials in order to explore domain formation, sometimes as a function of applied field,⁴ and has investigated the basic physics of superconductors⁵ and colossal magnetoresistive (CMR) manganites.^{6–14}

The idea that phase separation is crucial in explaining the CMR effect in manganites is now widely accepted. In many of these materials, the formation of conducting ferromagnetic pathways in an insulating background depends strongly on the magnetic field and temperature history. A real-space probe serves to verify this phase separation and link the microscopic picture to bulk magnetization and electrical transport data. Large-scale (micrometer-scale) phase separation consisting of a mixture of ferromagnetic and antiferromagnetic phases was first seen in the $\text{La}_{5/8-y}\text{Pr}_y\text{Ca}_{3/8}\text{MnO}_3$ (LPCMO) system at low temperature by Uehara *et al.* The authors created real-space phase maps by exploiting the difference in dark-field electron microscopy contrast between the charge-ordered antiferromagnetic and the charge-disordered ferromagnetic phases.¹⁵ Recently, MFM has been used to verify this phase separation and to study the phase transition as a function of field and temperature.¹⁶ Here we describe the use of high-field MFM to map out the temperature-dependent phase distribution of not only ferromagnetic and antiferromagnetic phases in LPCMO but also paramagnetic phases as well. This technique could be applied to any material system or fabricated device consisting of a mixture of phases with different magnetic properties.

The MFM used in this work has a cryogenic probe design, allowing for easy insertion into a superconducting magnet in a liquid He dewar.¹⁷ The tip on the MFM cantilever was sputter coated with $\text{Co}_{85}\text{Cr}_{15}$ to a thickness of 25 nm to make it sensitive to magnetic forces. During MFM imaging, the sample temperature can be varied from 5 to 250 K in an applied field. The single crystal LPCMO ($y=3/8$) sample was grown in a floating zone furnace, then cut, polished with

0.1 μm paper, and annealed at 1000 °C in an O_2 atmosphere for 10 h before being mounted inside the MFM.

The MFM imaging mechanism has been discussed in detail.^{2,18} We use the frequency modulation approach to MFM first outlined by Albrecht *et al.*¹⁸ In this scanning mode, the resonant frequency of the MFM cantilever is tracked as the MFM tip is scanned across the sample surface. Attractive interactions lead to negative frequency shifts of the lever. The resonant frequency shift of the lever is encoded as the contrast in the MFM images. In this work, we set the applied field H to be larger than the saturation field H_{sat} of the ferromagnetic phase and the saturation field of the MFM tip. Therefore, the magnetization M of the ferromagnetic or paramagnetic regions in the sample and the magnetization of the tip are aligned with the external field, leading to an attractive tip/sample interaction. Figure 1 illustrates this idea by showing a series of MFM images of a $5 \times 5 \mu\text{m}^2$ area of the LPCMO sample taken at 6 K with increasing H : Fig. 1(a), 0 T; Fig. 1(b), 0.16 T; and Fig. 1(c), 0.4 T. At this temperature, the sample is in the aforementioned phase-separated state; some regions are ferromagnetic and the remainder is antiferromagnetic. Figure 1(a), taken at zero field, shows contrast features arising from isolated ferromagnetic regions with randomly oriented magnetization, contrast pairs for in-plane domains, isolated bright and dark spots for mostly out-of-plane domains (marked by the black arrow), and more complicated structures for multidomain ferromagnetic regions (marked by the white arrow). As H is increased [Fig. 1(b)], the bright contrast regions turn to dark as each domain's magnetization is rotated parallel to H . If $H > H_{\text{sat}}$ as

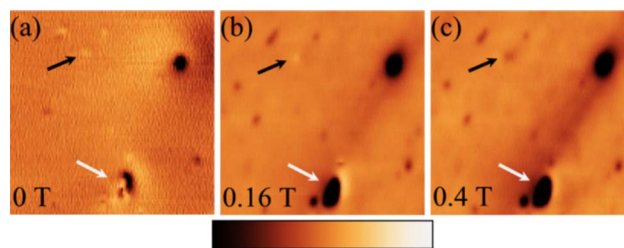


FIG. 1. (Color online) MFM images of the same $5 \times 5 \mu\text{m}^2$ area of the single crystal LPCMO sample taken at 6 K in an increasing applied field. The color scale spans 0.3 Hz for (a) and 2 Hz for (b) and (c). A single (multi-) domain ferromagnetic region is marked by the black (white) arrow.

^{a)}Electronic mail: delozanne@physics.utexas.edu

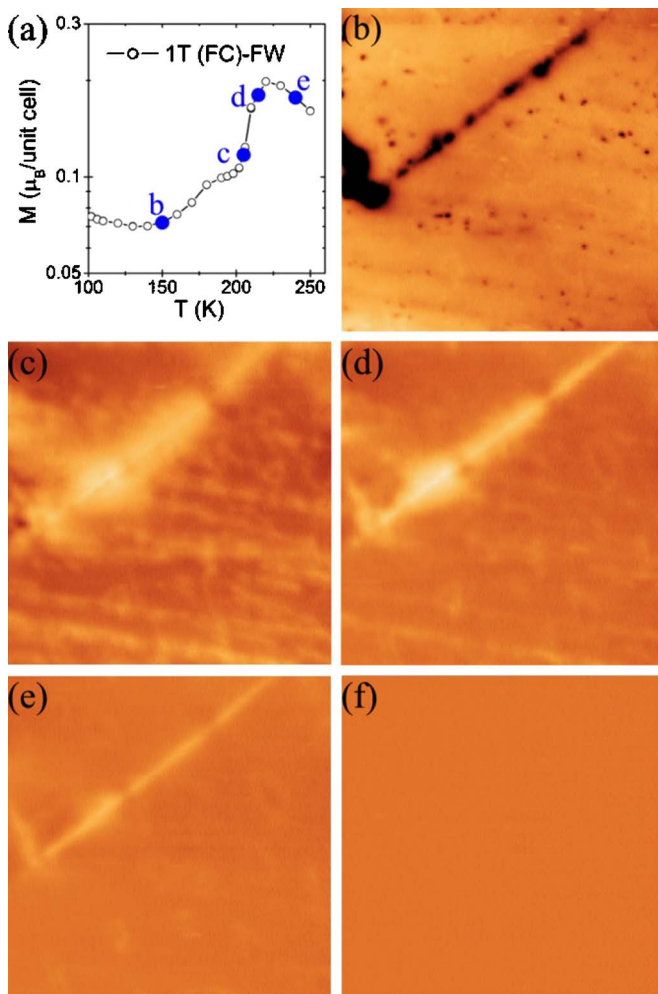


FIG. 2. (Color online) (a) Magnetization vs temperature for the LPCMO sample taken on field warming in a 1 T field after field cooling from room temperature to 5 K in a 1 T field. [(b)–(f)] MFM images of the same $9 \times 9 \mu\text{m}^2$ area of the single crystal LPCMO sample taken during warming. [(b)–(e)] are taken in a 1 T applied field at the temperatures shown in (a). (f) is taken in zero field at the same temperature as (e). The color scale spans 1.5 Hz for all MFM images.

in Fig. 1(c), the sample is magnetically saturated, and it is appropriate to identify the dark regions with the ferromagnetic phase and the surrounding bright regions with the antiferromagnetic phase.

In LPCMO we demonstrate discrimination between four distinctly different magnetic states, first between the charge-ordered antiferromagnetic (COAF) state and the ferromagnetic (FM) state, then between the high-temperature paramagnetic (PM) state and the charge-ordered paramagnetic (COPM) state. Each state is characterized by a different magnetic susceptibility, χ . Figure 2(a) shows the magnetization versus temperature plot for the LPCMO sample taken on field warming in a 1 T field after field cooling from room temperature to 5 K in a 1 T field. The plot focuses on two high temperature magnetic transitions. The first transition is from the COAF state to the COPM state and is evidenced by the kink at 180 K. The second transition is from the COPM state (lower χ) to the high-temperature PM state (higher χ) in the range of 205–240 K and is evidenced by the sharp rise in M . The closed circles are labeled according to the temperature at which MFM images [(b)–(e)] were taken during field warming of the sample in a 1 T field. The image shown in

Fig. 2(f) was taken at the same temperature as Fig. 2(e), but at zero field. All the MFM images show the same $9 \times 9 \mu\text{m}^2$ area of the sample and the color scale spans 1.5 Hz of resonant frequency shift.

The MFM image in Fig. 2(b) was taken below the antiferromagnetic transition temperature. In this region of phase space, the sample consists of a mixture of COAF regions and FM regions.¹⁵ The FM regions can be identified by the dark color in the MFM image, corresponding to a negative frequency shift due to the attractive tip/sample interaction. The MFM images in Figs. 2(c)–2(e) were taken after the temperature was increased past the antiferromagnetic transition temperature. In this temperature range, the sample is undergoing the transition from the COPM state to the high-temperature PM state. It has been shown that the COPM state has a lower χ than the high-temperature PM state.¹⁹ Partly based on the magnetization data from Fig. 2(a), in these images we associate the darker-colored (more attractive) regions with the phase with the higher χ , the high-temperature PM phase. Therefore, the brighter regions should correspond to regions which are still the COPM phase. The first conclusion we can draw from these three images is that phase separation is clear between the high-temperature PM and COPM phases and that the length scale for this separation can approach the micrometer range. The MFM image in Fig. 2(f) was taken at the same temperature as Fig. 2(e), but after H was reduced to zero. The lack of contrast seen in this control image is expected since the magnetization of the high-temperature PM and COPM regions has dropped to zero according to $M = \chi H$. For clues as to the origin of the last remaining COPM line seen in Fig. 2(e), we turn to optical microscopy.

By matching landmarks in optical microscopy images and large area topographic scans, we are able to align the MFM images with the optical images. In many cases more information can be gleaned from this alignment. One example of this is given in Fig. 3. Figure 3(a) is an optical image of the $36 \times 36 \mu\text{m}^2$ area of the LPCMO sample surrounding the scanned area in Fig. 2. Figure 3(b) is a polarized optical image of the same area. At temperatures below roughly 900 K, LPCMO possesses an orthorhombic distortion away from cubic symmetry and forms orthorhombic twins. The optical anisotropy of the orthorhombic lattice can be exploited to identify twin domains. The dark band near the bottom of Fig. 3(b) is a twin domain with a different distortion orientation than the surrounding material. The topography and MFM images shown in Figs. 3(c) and 3(d) come from the area outlined by the dashed white boxes in Figs. 3(a) and 3(b). The MFM image is reproduced from Fig. 2(c). Based on these aligned data layers, we can say that the last remaining COPM line seen in Fig. 2(e) coincides with a crack in the sample surface, implying that strain energy has a hand in determining the local phase transition temperatures for different areas of the sample. Indeed, there is mounting evidence that strain plays an important role in defining the balance between different phases in the CMR manganites.^{20–23}

In summary, a method for producing microscopic maps of magnetic phase distribution in magnetically phase-separated systems was presented. In a field greater than the saturation field for any present ferromagnetic phase, each phase will be uniformly magnetized, nonferromagnetic phases according to their susceptibilities, and the MFM contrast will change according to the local value of the magne-

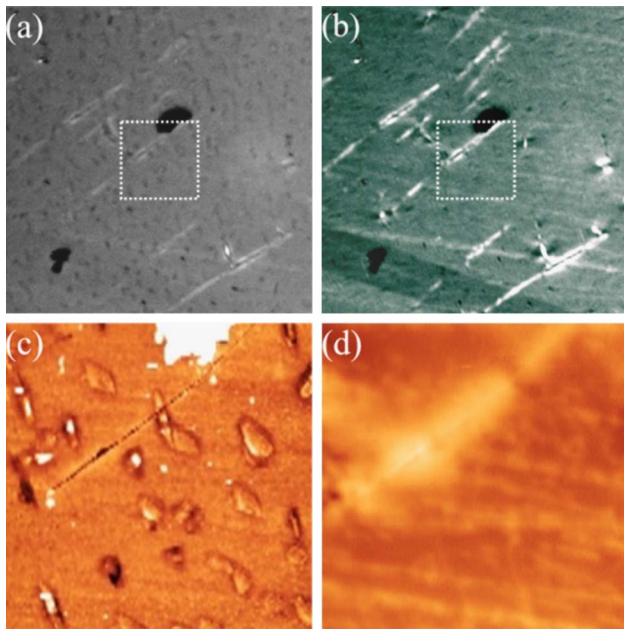


FIG. 3. (Color online) (a) Optical and (b) polarized optical microscopy images taken at room temperature of the same $36 \times 36 \mu\text{m}^2$ area of the LPCMO sample. (c) Topography and (d) MFM images taken at 210 K of the same $9 \times 9 \mu\text{m}^2$ area outlined by the white dashed box in (a) and (b). [MFM image is reproduced from Fig. 2(c).] The color scale spans 20 nm for (c) and 1.5 Hz for (d).

tization. This technique could be used to study magnetic phase separation/transitions in many different classes of materials, for example, other CMR manganites, the intermetallic compound Gd_5Ge_4 ,²⁴ Ru-doped CeFe_2 alloys,²⁵ disordered ferromagnets that show cluster glass behavior,^{26,27} or even systems engineered to be near the superparamagnetic limit through careful attention to size.²⁸

The authors gratefully acknowledge N. Hur, S. Park, and S.-W. Cheong for providing the LPCMO sample. This work was supported by NSF Grant No. DMR-0308575 and the Advanced Technology Program from the Texas Higher Education Coordinating Board.

¹Y. Martin and H. K. Wickramasinghe, *Appl. Phys. Lett.* **50**, 1455 (1987).

²D. Rugar, H. J. Mamin, P. Guethner, S. E. Lambert, J. E. Stern, I.

McFadyen, and T. Yogi, *J. Appl. Phys.* **68**, 1169 (1990).

³S. Y. Chou, *Proc. IEEE* **85**, 652 (1997).

⁴H. S. Nalwa, *Magnetic Nanostructures* (American Scientific, Stevenson Ranch, CA, 2002).

⁵A. de Lozanne, *Supercond. Sci. Technol.* **12**, R43 (1997).

⁶Q. Lu, C. C. Chen, and A. de Lozanne, *Science* **276**, 2006 (1997).

⁷C. Kwon, M. C. Robson, K.-C. Kim, J. Y. Gu, S. E. Lofland, S. M. Bhagat, Z. Trajanovic, M. Rajeswari, T. Venkatesan, A. R. Kratz, R. D. Gomez, and R. Ramesh, *J. Magn. Magn. Mater.* **172**, 403 (1997).

⁸Y.-A. Soh, G. Aeppli, N. D. Mathur, and M. G. Blamire, *Phys. Rev. B* **63**, 020402 (2000).

⁹M. E. Hawley, G. W. Brown, P. C. Yashar, and C. Kwon, *J. Cryst. Growth* **211**, 86 (2000).

¹⁰R. Desfeux, S. Bailleul, A. D. Costa, W. Prellier, and A. M. Haghiri-Gosnet, *Appl. Phys. Lett.* **78**, 3681 (2001).

¹¹Y. Wu, Y. Matsushita, and Y. Suzuki, *Phys. Rev. B* **64**, 220404 (2001).

¹²L. Zhang, C. Israel, A. Biswas, R. L. Greene, and A. de Lozanne, *Science* **298**, 805 (2002).

¹³J. Dho, Y. N. Kim, Y. S. Hwang, J. C. Kim, and N. H. Hur, *Appl. Phys. Lett.* **82**, 1434 (2003).

¹⁴A. Schwarz, M. Liebmann, U. Kaiser, R. Wiesendanger, T. W. Noh, and D. W. Kim, *Phys. Rev. Lett.* **92**, 077206 (2004).

¹⁵M. Uehara, S. Mori, C. H. Chen, and S.-W. Cheong, *Nature (London)* **399**, 560 (1999).

¹⁶W. Wu, C. Israel, N. Hur, S. Park, S.-W. Cheong, and A. de Lozanne, *Nat. Mater.* (submitted).

¹⁷C. Israel, C. Hyun, A. de Lozanne, S. Phark, and Z. G. Khim, *Rev. Sci. Instrum.* **77**, 23704 (2006).

¹⁸T. R. Albrecht, P. Grütter, D. Horne, and D. Rugar, *J. Appl. Phys.* **69**, 668 (1991).

¹⁹P. A. Sharma, S. B. Kim, T. Y. Koo, S. Guha, and S.-W. Cheong, *Phys. Rev. B* **71**, 224416 (2005).

²⁰Y. Suzuki, H. Y. Hwang, S.-W. Cheong, and R. B. van Dover, *Appl. Phys. Lett.* **71**, 40 (1997).

²¹A. J. Millis, T. Darling, and A. Migliori, *J. Appl. Phys.* **83**, 1588 (1998).

²²A. Biswas, M. Rajeswari, R. C. Srivastava, T. Venkatesan, R. L. Greene, Q. Lu, A. L. de Lozanne, and A. J. Millis, *Phys. Rev. B* **63**, 184424 (2001).

²³Y.-A. Soh, P. G. Evans, Z. Cai, B. Lai, C.-Y. Kim, G. Aeppli, N. D. Mathur, M. G. Blamire, and E. D. Isaacs, *J. Appl. Phys.* **91**, 7742 (2002).

²⁴M. K. Chattopadhyay, M. A. Manekar, A. O. Pecharsky, V. K. Pecharsky, K. A. Gschneidner, J. Moore, G. K. Perkins, Y. V. Bugoslavsky, S. B. Roy, P. Chaddah, and L. F. Cohen, *Phys. Rev. B* **70**, 214421 (2004).

²⁵S. B. Roy, G. K. Perkins, M. K. Chattopadhyay, A. K. Nigam, K. J. S. Sokhey, P. Chaddah, A. D. Caplin, and L. F. Cohen, *Phys. Rev. Lett.* **92**, 147203 (2004).

²⁶J. A. Mydosh, *Spin Glasses* (Taylor & Francis, London, 1993).

²⁷B. Coles, B. V. B. Sarkissian, and R. H. Taylor, *Philos. Mag. B* **37**, 489 (1978).

²⁸E. Gu, S. Hope, M. Tselepi, and J. A. C. Bland, *Phys. Rev. B* **60**, 4092 (1999).